Lawrence Berkeley National Laboratory
Chemical Sciences

Title
Crystal misorientation correlates with hardness in tooth enamels

Permalink
https://escholarship.org/uc/item/4z44k6c8

Authors
Stifler, Cayla A
Jakes, Joseph E
North, Jamie D
et al.

Publication Date
2021

DOI
10.1016/j.actbio.2020.07.037

Peer reviewed

Crystal misorientation correlates with hardness in tooth enamels✩☆

Cayla A. Stifler[a], Joseph E. Jakes[b], Jamie D. North[c], Daniel R. Green[d], James C. Weaver[e], Pupa U.P.A. Gilbert[a,f,1,*]

[a] Department of Physics, University of Wisconsin, Madison, WI 53706, United States
[b] Forest Biopolymers Science and Engineering, USDA Forest Service, Forest Products Laboratory, Madison, WI 53726, United States
[c] Department of Chemistry, Carleton College, Northfield, MN 55057, United States
[d] Department of Human Evolutionary Biology, Harvard University, Cambridge, MA 02138, United States
[e] Wyss Institute for Biologically Inspired Engineering, Harvard University, Cambridge, MA 02138, United States
[f] Departments of Chemistry, Geoscience, Materials Science, University of Wisconsin, Madison, WI 53706, United States

ARTICLE INFO

ABSTRACT

The multi-scale hierarchical structure of tooth enamel enables it to withstand a lifetime of damage without catastrophic failure. While many previous studies have investigated structure-function relationships in enamel, the effects of crystal misorientation on mechanical performance have not been assessed. To address this issue, in the present study, we review previously published polarization-dependent imaging contrast (PIC) maps of mouse and human enamel, and parrotfish enameloid, in which crystal orientations were measured and displayed in every 60-nm-pixel. By combining those previous results with the PIC maps of sheep enamel presented here we discovered that, in all enamel(oid)s, adjacent crystals are slightly misoriented, with misorientation angles in the 0°-30° range, and mean 2°-8°. Within this limited range, misorientation is positively correlated with literature hardness values, demonstrating an important structure-property relation, not previously identified. At greater misorientation angles 8°30°, this correlation is expected to reverse direction, but data from different non-enamel systems, with more diverse crystal misorientations, are required to determine if and where this occurs.

Statement of Significance

We identify a structure-function relationship in tooth enamels from different species: crystal misorientation correlates with hardness, contributing to the remarkable mechanical properties of enamel in diverse animals.

1. Introduction

1.1. Structure-function relationships

Since its infancy, the field of paleontology has sought to understand the function of fossilized bones and teeth based on their structure. Indeed, Georges Cuvier, the father of paleontology, believed that the structure of each component of any animal was inextricably linked to its function, and wrote in 1840 that these links show "general laws, as demonstrable as those which are derived from calculation or experiment" [1]. Thus, nearly 200 years ago, scientists understood the importance of investigating structure-function relationships in biological materials. Tooth enamel, for example, has evolved structures at every length scale to meet the specific needs and functions of the animal, whether those are chewing tough plants, piercing and tearing off flesh, or crushing hard skeletal parts. In a representative 1974 study, Wolf-Ernst Reif classified shark tooth morphologies based on their function, and described how their microstructural designs supported each function [2]. Exploring these detailed multi-scale structure-function relationships in enamel enriches our understanding of what makes this biological material among the hardest and most durable tissues in extant species during life, and in extinct species long after death.
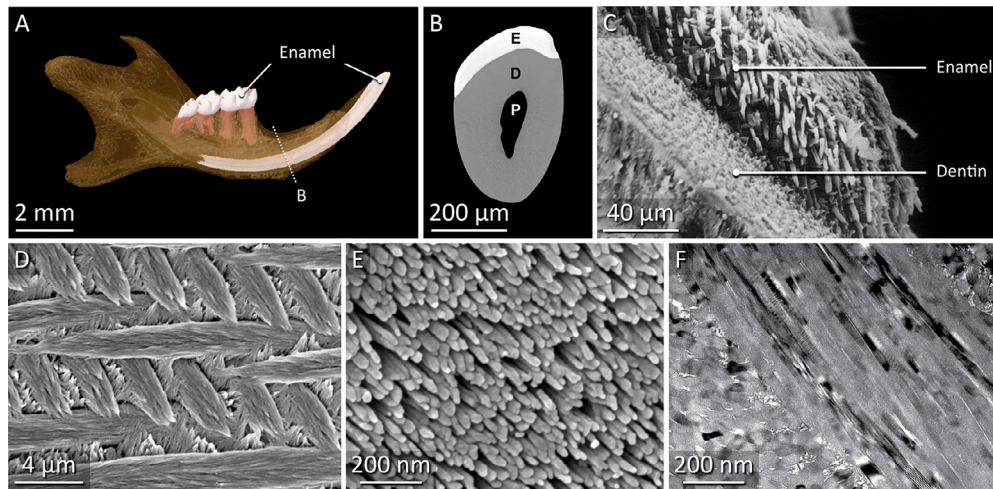
Fig. 1. Hierarchical structure of mouse and rat enamel. (A) Mandible (lower jaw) of a mouse showing the incisors and molars, adapted from Phil Salmon at Bruker and [128]. (B) Cross section of mouse mandibular incisor cut along the line indicated in (A) showing the enamel = E, dentin = D, and the pulp = P. Note that the surrounding bone is not shown in this cross section. Adapted from [128]. (C) Scanning electron microscope (SEM) image of a growing rat incisor showing immature enamel and dentin adapted from [50]. (D) SEM image of decussating mouse enamel. (E) SEM image of elongating, parallel HAP nanocrystals in mouse enamel. (F) Transmission electron microscopy image of HAP nanocrystals in mouse enamel. D and E adapted from [51] and F from [129].

1.2. Hierarchical structure of enamel

As with many other biominerals, the hierarchical organization of enamel, which combines hard, brittle hydroxyapatite $(Ca_{10}(PO_4)_6(OH)_2)$ (HAP) with strategically placed soft, flexible organics in a highly organized structure spanning multiple length scales, is responsible for enamel's remarkable mechanical properties [3]. In the present study, it should be noted that the abbreviation HAP does not simply refer to pure HAP, but also includes and encompasses all the frequent atomic substitutions in hydroxyapatite that are encountered in the teeth of diverse animal species [4-13]. Each hierarchical level of enamel's structure has distinct functional purposes [14], and these levels, from the macro-scale to the nano-scale, are described in more detail in the following subsections and are demonstrated in Fig. 1.

1.2.1. Dentition

At the largest structural length scale, dentition refers to the arrangement of teeth in the mouth in a particular species [15]. While this level of structure has been studied for centuries, as it is observable with the naked eye (see Fig. 1A), recent studies still offer new insights. For example, observations of modern and prehistoric human dentition show differences in wear attributable to changes in how the teeth occlude, during the transition from a hunter gatherer to an agricultural society [16]. The examination of dentition is also important in determining how animals process food. Modeling and experimental work, for example, have shown that an elongated tooth shape in sheep molars helps them resist fracture [17], and their characteristically continuously erupting growth mode is highly correlated with grazing behavior, counteracting the destructive effects of abrasive plant materials and soil particles ingested during feeding [18]. In a non-mammalian example, through the analysis of parrotfish pharyngeal tooth shape and wear patterns, Carr *et al.* were able to deduce how the pharynx moves to mill coral skeletons [19].

1.2.2. Dental tissue

Vertebrate teeth contain four different kinds of dental tissues: enamel, dentin, cementum, and pulp (see Fig. 1B). Enamel is the outermost, last-formed layer, and is 97% mineral by weight, mainly HAP [20], with enamel proteins playing an important role

in enamel formation and patterning [21-24]. Dentin is less mineralized than enamel, at 70 w%%, and characterized by the presence of tubules [25,26]. Each tubule is surrounding by a layer of mineralized, but non-collagen-containing peritubular dentin [25,26], which is in turn, surrounded by intertubular dentin consisting of mineralized collagen fibrils. Near the boundary between dentin and enamel, the tubules contain no peritubular dentin and are thought to cushion enamel during mechanical loading [27]. Cementum is slightly less mineralized than dentin, at 65 w% mineral, and it connects the root of the tooth to the jawbone and ligaments [20,26]. Cementum contains mineralized collagen and other proteins, and, in human teeth, grows in thickness over a lifetime [28]. The pulp is a completely soft tissue at the center of the tooth, and contains blood vessels and nerves [20]. In some fish, such as sharks and parrotfish, the outer tooth layer is made of fluorapatite (FAP, $Ca_{10}(PO_4)_6F_2$) crystals, and is termed enameloid [29]. Notable exceptions are seen in the living lobed fin fish, (*Latimeria* spp*.),* which have true enamel, and in some genera of ray-finned fish (*Polypterus* and *Lepisosteus*), in which enamel covers the tooth shaft and is called collar enamel [30].

1.2.3. Rods and the higher-order patterns they create

Rods, previously called prisms, are cylindrical bundles of nearly aligned HAP nanocrystals (described in more detail in Section 1.2.4) with discontinuous organics on one side, and contain trace amounts of water [20,23,31]. The crystals surrounding the rods are called interrod or interprismatic enamel [32]. Generally, the rods are 2–10 μm in diameter and hundreds of microns long [32,33], and their shape and arrangement are species-specific. Some primates, such as lemurs, for example, have rods with perfectly circular cross-sections with fully encapsulated by interrod enamel that completely separates each rod from its neighbors (sometimes called pattern 1) [34-37]. In contrast, human enamel rod cross-sections are keyhole-shaped, with a round head portion and an elongated tail portion that makes up the interrod as shown in Fig. 2A (pattern 3) [35-40]. In sheep and other species, the enamel rods, by contrast, are not as well defined and resemble partially overlapping circles when viewed in section (pattern 2) [34]. The enamel from crocodiles has no rods whatsoever, and as such, is described as aprismatic enamel [34]. Instead of rods, fish enameloid has bundles, groups of elongated FAP crystals with their elongation directions roughly aligned [2,29].
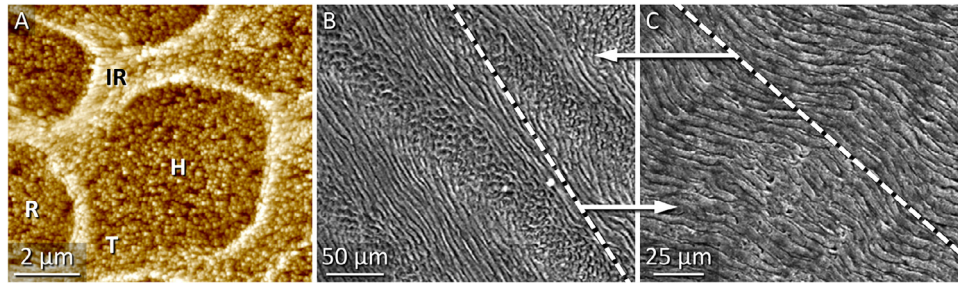
Fig. 2. Human enamel at two different length scales. (A) Atomic force microscopy image of the keyhole shape of human rods. *R*=rod, IR=interrod, also known as *H*=head, and *T*=tail of rod. Each rod and interrod, formed by a single ameloblast cell, looks like a keyhole, where the small part of the keyhole, the IR, is determined and confined by two adjacent Rs. Notice that the R gradually and seamlessly turns into the IR in each keyhole structure, whereas the transition IR to R is abrupt, and delimited by a thick organic sheath. Adapted from reference [24]. (B, C) SEM images of decussating enamel, sectioned along directions similar to the dashed white lines in C and B, respectively. (B, C) Adapted from [45].
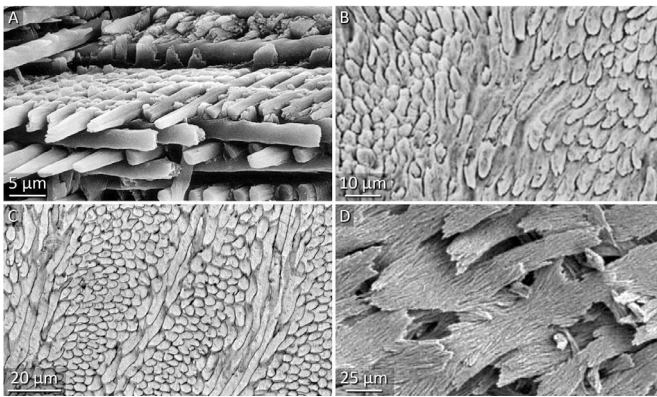

Fig. 3. SEM images of enamel rods from (A) rat, (B) human (C) sheep enamel, and (D) enameloid bundles from parrotfish enameloid. (A), (B), and (D) adapted from references [50,130], and [54], respectively.

Enamel zones that contain rods arranged nearly parallel to one another are called radial enamel, whereas rods that are arranged in regularly alternating groups or layers are known as decussating enamel [32,35–37]. To decussate means to cross or intersect each other to form an X. Perhaps the most familiar decussation pattern is found in human enamel, resulting the presence of features known as Hunter-Schreger bands. In these bands, the rods' elongation direction gradually rotates 90° over approximately 15 layers and then changes back, gradually, in a periodic pattern (see Figs. 2B-C, 3B, and 4B) [34,38,39,41–45]. The human "decussation angle", therefore, is 90°. Although the shape of individual rods is different, the decussation pattern and angle in sheep enamel is similar to human: the rods' elongation direction rotates gradually by 90° back and forth across the inner enamel thickness (see Figs. 3C and 4C) [34,46]. In mouse and rat enamel, by contrast, layers of parallel rods are stacked, alternating as ABABAB, with rods in A and B layers at a decussation angle of 70° (see Figs. 1C, 3A and 4A) [47–51]. In more complex enamels, there can be a mixture of prismatic and aprismatic enamel and even a mixture of different patterns, giving an additional hierarchical level of structure to those enamels [37]. For example, sheep have radial enamel at the surface of the tooth, decussating enamel in the middle, and near the dentin enamel junction (DEJ), sheets of interrod enamel are interspersed between groups of aligned rods [46].

In parrotfish enameloid, the bundles are interwoven in a complex, tangled pattern (see Figs. 3D and 4D-G) [52–54]. The bundles are thin and tightly woven together near the tip of the tooth, and the bundle diameter increases moving closer to the dentin [53]. Despite the existence of numerous studies investigating enamel ultrastructure across multiple species, the complex

three-dimensional geometry of its decussation is not yet fully understood.

1.2.4. Nanocrystals or crystallites

At the nanoscale, enamel is composed of acicular HAP crystals that are approximately 25 nm by 60 nm in cross-section and hundreds of microns long [33,45,55–58,132]. Such nanocrystals form the micro-scale structure of enamel, including rod, interrod, and aprismatic enamel, as well as fish enameloid bundles. Fish enameloid nanocrystals generally exhibit this same acicular geometry, but are instead composed of FAP [29,52]. These nanocrystals tend to have a preferred crystallographic orientation as observed by numerous x-ray diffraction studies [59-64], one that can even be partially recovered during remineralization studies in the presence of fluorine and amelogenin [64,65]. Transmission electron backscattered diffraction (tEBSD) [66] and Polarization-dependent Imaging Contrast (PIC) mapping techniques, previously developed for carbonates [67-69], have also been employed to determine how enamel crystals are oriented with respect to their elongation direction and rod structures [53,70,71]. Surprisingly, Beniash *et al.* showed that the elongation direction of the nanocrystals and their crystallographic *c*-axis orientation are not parallel to one another [71]. This observation was surprising because synthetic FAP crystals grown *in vitro* invariably show that the crystals elongate along their *c*-axes [72]. Fig. 5 shows synthetic and biogenic single crystals, demonstrating this unexpected difference.

1.3. Measurable mechanical properties are tied to structure

In an attempt to understand the functional significance of its hierarchical structure, several previous studies have investigated the roles of specific enamel features on its bulk mechanical properties [73-76]. As the outermost layer of teeth, enamel must withstand hundreds of Newtons of force many times a day, and last a lifetime [77]. Even though it is primarily composed of a calcium-based mineral, the stress-strain behavior, creep response, and fracture behavior of enamel are more akin to metals like gold than to geologic apatite [78]. The specific elongation direction of rods, and its impact on mechanical properties [79-81] and wear [82], has also been investigated, revealing that the interrod inelastic energy dissipation is higher than in rod enamel [83]. Enamel hardness and elastic modulus also decrease from the surface of the tooth to the DEJ [84,85], and older enamel at the tooth surface is harder and stiffer than younger enamel [86]. Lastly, hardness and elastic modulus are both higher when the loading direction is parallel to the rod's elongation direction than perpendicular to it [44]. Multiple studies on human enamel have examined how the hierarchical structure contributes to enamel's remarkable fracture toughness, stress-strain behavior, and resistance to crack
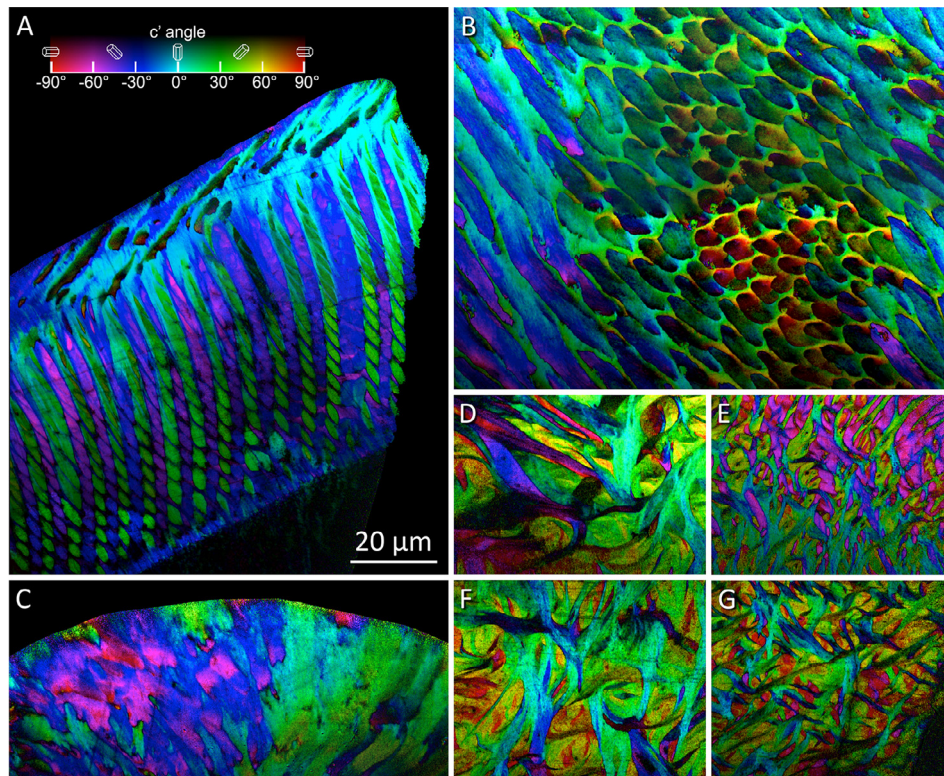
Fig. 4. Polarization-dependent imaging contrast (PIC) maps of enamel from mouse (A), human (B), sheep (C), and enameloid from parrotfish (D–G). In all four species, the *c*-axis orientation of the HAP or FAP crystals is not always aligned with the elongation direction of crystals in the enamel rods or bundles. Across a single rod or bundle, HAP or FAP crystals are slightly misoriented to different extents in different species: mouse is the most cooriented, while parrotfish the most misoriented. All data except for C were previously published. Mouse, A, from [70], human, B, from [71], and parrotfish, D-G, from [53]. The 20-µm scalebar applies to all PIC maps.
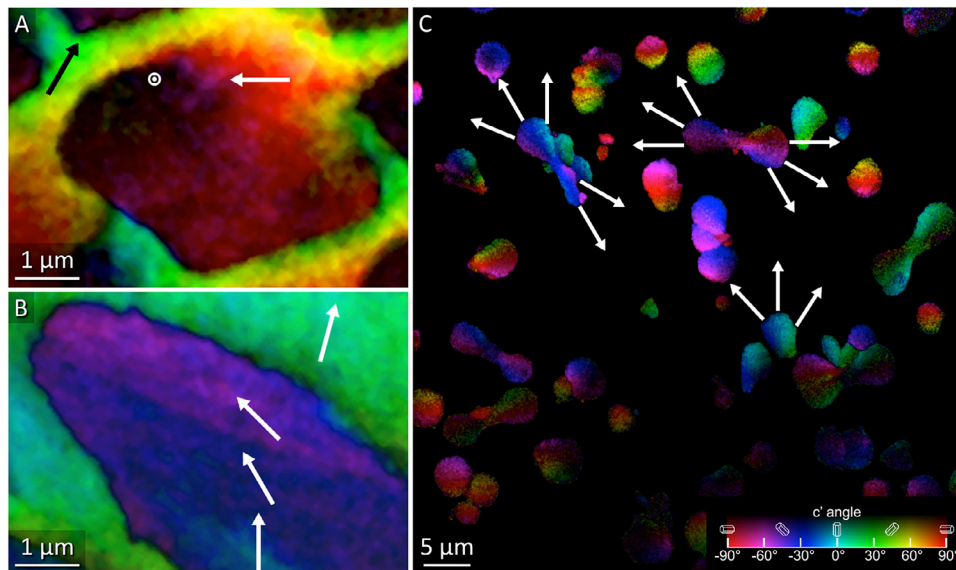

Fig. 5. PIC maps of (A and B) selected human enamel rods from the PIC map in Fig. 4B [71], and (C) synthetic fluorapatite dumbbells. (A) A rod with its long axis perpendicular to the image plane contains nanocrystals with *c*-axis orientations gradually changing from 90° out of the polarization plane (black pixels in PIC maps) to in-plane (red), as indicated by an out-of-plane arrow (concentric circles) and the horizontal white arrow. This is a ~90° out-of-plane rotation. The interrod *c*-axis orientation is indicated with a black arrow. (B) Another rod with its long axis parallel to the image plane containing nanocrystals with *c*-axes indicated by white arrows. (C) The *c*-axes of the nanocrystals in fluorapatite dumbbells correspond to their radial orientation, in contrast to enamel.

propagation [75,76,87]. For example, a study investigating enamel cracks originating at the DEJ found that they rarely result in large-scale tooth failure [88]. Furthermore, the mechanical properties of enamel have been found to be anisotropic. At the whole-tooth scale, wear testing of successive layers of enamel were found to have different shear velocity components during grinding, demon-strating different resistance to wear for the different layers [89], and tooth numerical modeling reveals how variations in properties like the elastic modulus can help dissipate applied stresses [90]. At the rod scale, several studies have found hardness, elastic modu-lus, fracture toughness, crack propagation, and shear behavior to vary for tests carried out in different loading directions relative

to the rod elongation direction [44,74,91–94]. Although FAP and HAP pure minerals have different physical properties [95,96], many shark species like bonnethead sharks, sand tiger sharks [97], and great white sharks [98] have fluorapatite enameloid with hardness in the 3–5 GPa range in most tooth locations, which have hardness values similar to human and sheep enamel. Since the mechanical properties are similar, including both enamel and enameloid teeth in the same comparative plots, as in the present study, is justified.

1.4. Motivation for this analysis

While many previous studies have investigated the relationship between rod elongation direction in decussation patterns and crack propagation, there is no direct experimental evidence available on how intra-rod crystal coorientation or misorientation correlates with any mechanical properties. Despite this lack of direct experimental evidence, molecular dynamics simulations from Beniash *et al.* 2019 demonstrate that small misorientations deflect cracks better than larger or no misorientations [71].

Here, we hypothesize that enamel hardness correlates with the extent of crystal misorientation, which motivated the analysis of previously published PIC maps from mouse, human, and parrotfish enamel(oid) and previously published nano-hardness values. The results from these studies are organized into the plots reported here, to explore the correlation of the two parameters: one structural, crystal misorientation, and one functional, the hardness.

We also include here mechanical testing data from sheep teeth, which, although not previously published, exhibit the same trends, and thus strengthen the validation of the hardness-misorientation relationship hypothesized and tested here. While the hardness and elastic modulus of sheep enamel has been reported previously [99], those studies were performed on old and worn teeth. To eliminate the complications associated with the investigation of old and worn teeth, we instead conducted our own nanoindentation measurements on young and pristine teeth sheep teeth (see Section 4.4 for details).

2. Results

Surprisingly, the *c*-axis orientations of the nanocrystals do not always correspond with the elongation direction of the rod in all enamels presented here. Indeed, the difference between the long axis of the rod and the crystal orientation can be quite dramatic. Since mouse rods are circular in cross-section, once embedded and polished, their ellipticity can be used to infer their tilt angle relative to the polished surface. In the sample shown in Fig. 4A, for example, the sectioned green rods at the bottom of the image have their long axes at −30° from vertical but the PIC map indicates that the *c*-axis orientation is at +30° from vertical (green). In human enamel (Fig. 4B), the predominantly cyan rods are not vertical as expected, but closer to −30° from vertical. The green rods in sheep enamel (Fig. 4C) range from +30° to −15° from vertical in elongation direction, even though the *c*-axes are all aligned at +30°. Similarly, the dark blue bundles in parrotfish enameloid (Fig. 4F-G) have their *c*-axes oriented at −30° from vertical but are elongated −60°–0° from vertical. Fig. 5 shows two individual rods from Fig. 4B at a higher magnification along with synthetic fluorapatite dumbbells and the contrast is striking. The *c*-axes orientations of the nanocrystals in the human rods gradually shift from being aligned with the rod direction to 90° from it (Fig. 5A), while in the dumbbell nanocrystals the *c*-axes orientation exactly matches their elongation direction. A detailed description on the interpretation of PIC maps is included in Section 4.2. To minimize confusion, we clarify that all angles described in the text are with respect to the polarization plane, not the image plane.

The local misorientation in a PIC map can be described by a parameter called misorientation Δc, which is the angular distance in three dimensions between the crystalline *c*-axes in two adjacent 60 nm-pixels [71,100,101]. For example, if the *c*-axis of the crystal in one pixel is oriented at 30° and the one in the adjacent pixel at 40°, the misorientation Δc is 10°. Because the nanocrystals are ~60 nm in size, and the pixels are 60 nm in size, the two are well-matched, thus the physical meaning of Δc is simply the misorientation angle of any two immediately adjacent nanocrystals. As shown by Beniash *et al.*, in enamel, the *c*-axes of the crystals do not coincide with their long axes, thus the misorientation Δc is a measure of the crystalline misorientations and not a measure of rod direction [71].

We stress that the misorientation angle Δc is a direct, quantitative, and 3D measurement, and is not based on any assumptions. It is not at all dependent on the elongation direction of crystals, and is obtained by rotating the polarization direction of the illuminating x-ray photons. It is thus equivalent to polarized light microscopy of birefringent crystals in the visible range, but provides higher spatial resolution and surface sensitivity [102].

The distributions for each of the four model species (Fig. 6A-D) indicate that misorientation Δc is below 30° for nearly every pixel pair, so the overall misorientation is relatively small. Within the 30° angle spread of almost all adjacent pixel pairs, at least 95% of the misorientations are between 0 and 10°, meaning that these misorientations are much more frequent compared to the <5% abundance in the 10–30° range. Mouse enamel has the lowest mean misorientation, as all the crystals in each rod are nearly perfectly co-oriented near the DEJ, and less co-oriented near the tooth surface. In contrast, the intricately tangled bundles that make up parrotfish enameloid show the highest mean misorientation.

In order to assess how well the misorientation and hardness correlate, we performed a linear fit of all the data points. Since there is no theory yet behind this correlation, other non-linear fits were neither expected nor observed. For any linear fit, the correlation coefficient *R* provides a quantitative estimate of the goodness of the fit, varying from 0 to 1. In experiments involving biological or medical materials, which are typically characterized as complex multi-component systems, two parameters are considered correlated if their correlation coefficient exceeds the minimum threshold $R > 0.30$ [103]. For enamel(oid), despite its comparatively low $R = 0.51$ for the hardness and mean misorientation fit in Fig. 7A, these two parameters Section 4.5 can be still be considered correlated with a probability $p = 0.000059$, which corresponds to 4.0 σ significance (see Methods Section 4.5). The hardness increases linearly from 3 GPa to 7 GPa, as the mean misorientation increases from 2° to 8°. PIC maps of sheep, mouse, and parrotfish enamel(oid) used in the misorientation analysis were acquired from only one individual, whereas the human misorientation data came from three different individuals, labeled human tooth 1, human tooth 2, and human tooth 3 in the figure legend. For some of the points, we used multiple hardness and elastic modulus values for a single measured misorientation if multiple references measured *H* and *E* at similar locations. Nanoindentation *H* and *E* data for mouse were taken from Pugach *et al.* 2013 and White *et al.* 2007 [104,105]. Human enamel *H* and *E* data were taken from Braly *et al.* 2007, Cuy *et al.* 2002, Barbour *et al.* 2003, and Park *et al* 2008 [79,84,86,106]. Parrotfish H and E data were taken from Marcus *et al.* 2017 [53]. We measured H and E for sheep and the human data points indicated in the legend, as described in the methods section. The elastic modulus (Fig. 7B) also ($R = 0.44$, $p = 0.00098$, 3.3 σ significance, correlates with the mean misorientation, linearly increasing from 58 GPa to 124 GPa, as the misorientation increases in the same 2°–8° range as the hardness. This result is not surprising per se, as the elastic modulus and hardness are related, but the slopes are very different:
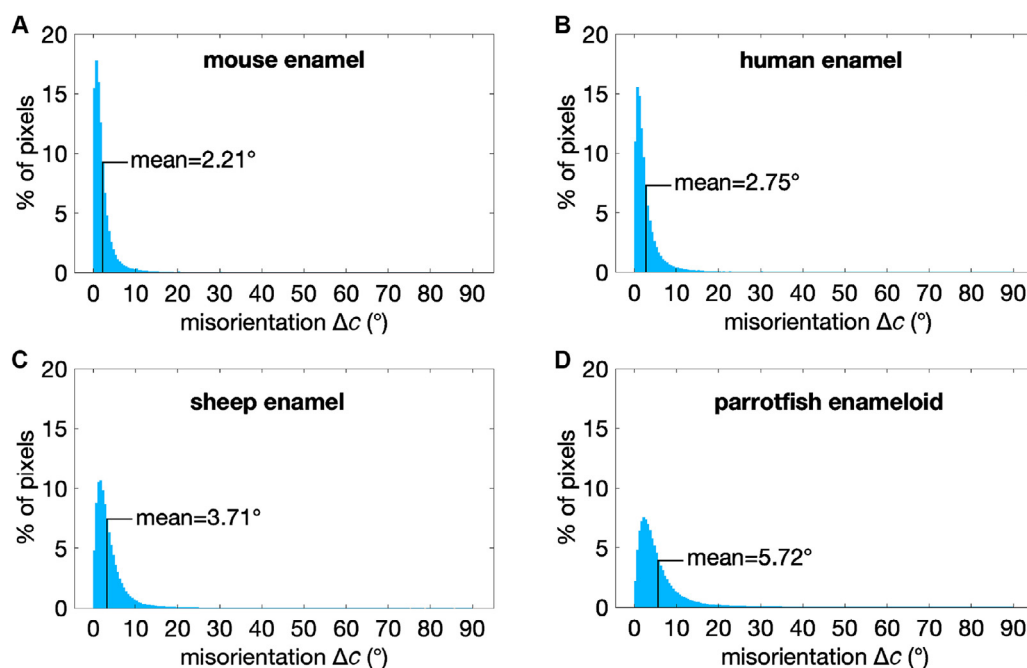
Fig. 6. Histograms showing the distribution of the angular distances Δc (= misorientation Δc) between the c-axes of the crystals in two adjacent pixels, calculated for the PIC maps in Fig. 4 ($>10^6$ pixel pairs per image are included in each histogram), correspondingly positioned and labeled: (A) mouse, (B) human, (C) shark, (D) parrotfish. Mouse enamel has the lowest mean misorientation Δc, parrotfish enameloid has the highest mean misorientation Δc, substantiating and quantifying the visually observed misorientations in PIC maps.

0.4 GPa/° for H vs. misorientation and 4.9 GPa/° for E vs. misorientation. There are multiple points for human, sheep, and parrotfish enamel(oid)s in Fig. 7 because the hardness varies with location within each tooth, thus the hardness used corresponds to the value at the location where each specific PIC map was acquired. The H and E values obtained from sheep and the human-tooth-3 data points in Fig. 7 were acquired at precisely the same locations as their corresponding PIC maps and measured Δc values. For some of the published PIC maps analyzed here, H and E values were not previously measured but were instead taken from the literature, carefully ensuring that they were measured at the same normalized distance from the DEJ as the PIC map was acquired and the measured Δc.

Enamel(oid)s are consistently harder at the surface and softer near the DEJ, and misorientation follows the same trend. In both human and parrotfish enamel(oid), for which many literature datapoints are available, gradual changes in misorientation correspond to gradual changes in hardness. For example, the tips of the parrotfish teeth in Fig. 4E and 4G are more misoriented and harder than corresponding areas near the DEJ in Fig. 4D and 4F. Unlike the other investigated species reported here, the hardness of mouse enamel does not appear to correlate with distance from the DEJ, as confirmed by White *et al.* 2007 [105]

In contrast to the mean misorientation, the Ca/P molar ratio does not correlate with hardness ($R = 0.04$, $p = 0.73$), as shown in Fig. 7C. For human enamel, the hardness data from Braly *et al.* 2007, Barbour *et al.* 2003, and Park *et al.* 2008 [79,86,106] were each paired with Ca/P ratios from Ngo *et al.* 1997, Kodaka *et al.* 1992, and Robinson, Weatherell, and Hallsworth 1971 [9,11,12] in Fig. 7C because these references only contained either hardness or Ca/P ratios, but not both. The human enamel data points taken from Cuy *et al.* 2002 [84], reported both hardness and CaO and P_2O_5 w% for the same tooth, so no additional references were necessary for these points. The CaO and P_2O_5 w% were converted into molar percentages using stoichiometry and the molar mass of CaO,

P_2O_5, Ca, and P and dividing the Ca molar percentage by the P percentage. Ca/P ratios for mouse enamel were taken from Hu *et al.* 2015 [107] and hardness from Pugach *et al.* 2013 and White *et al* 2007. [104,105]. Sheep enamel Ca/P ratios came from Dios Teruel *et al.* 2015 and Barnicoat 1959 [8,10] and the hardness was measured in the present study. For simplicity, all human H values have the same color in Fig. 7C. The Ca/P molar ratio is indicative of substitutions to calcium and phosphorus, the main components of apatite. For stochiometric apatite, the Ca/P molar ratio is 1.67, and it is clear for the data in Fig. 7C that all of the data points values are between 90% and 100% of this ratio. These results demonstrate that there are few cation substitutions to calcium and none to phosphorus in enamel apatite, and that such substitutions, when they occur, are not correlated with hardness.

3. Discussion

Geologic apatite single crystals have been shown to have better mechanical performance along the c-axis, when indenting the (0001) facet, than perpendicular to the c-axis, when indenting the (1010) facet. Specifically, the (0001) facet has hardness, elastic modulus, and work hardening rate coefficient of 7.06 GPa, 150.38 GPa, and 18.82 GPa, respectively. The (1010) facet has 6.41 GPa, 143.56 GPa, and 14.47 GPa, respectively [108,109]. Enamel has been shown to have anisotropic properties as described in Section 1.3, and therefore, two slightly misoriented crystals have slightly different hardness values. Previous molecular dynamics (MD) simulations [71] showed that crack deflection occurs at a smaller misorientation of 14.1°, and not at larger or zero misorientations. Thus, small ($<30°$) misorientation angles observed in all of the species reported here may also provide better crack-deflection and therefore higher fracture toughness, than for larger misorientation angles ($>30°$).

Within the smaller ($<30°$) misorientation angles, however, not all angles are equal, from a mechanical performance point of view.
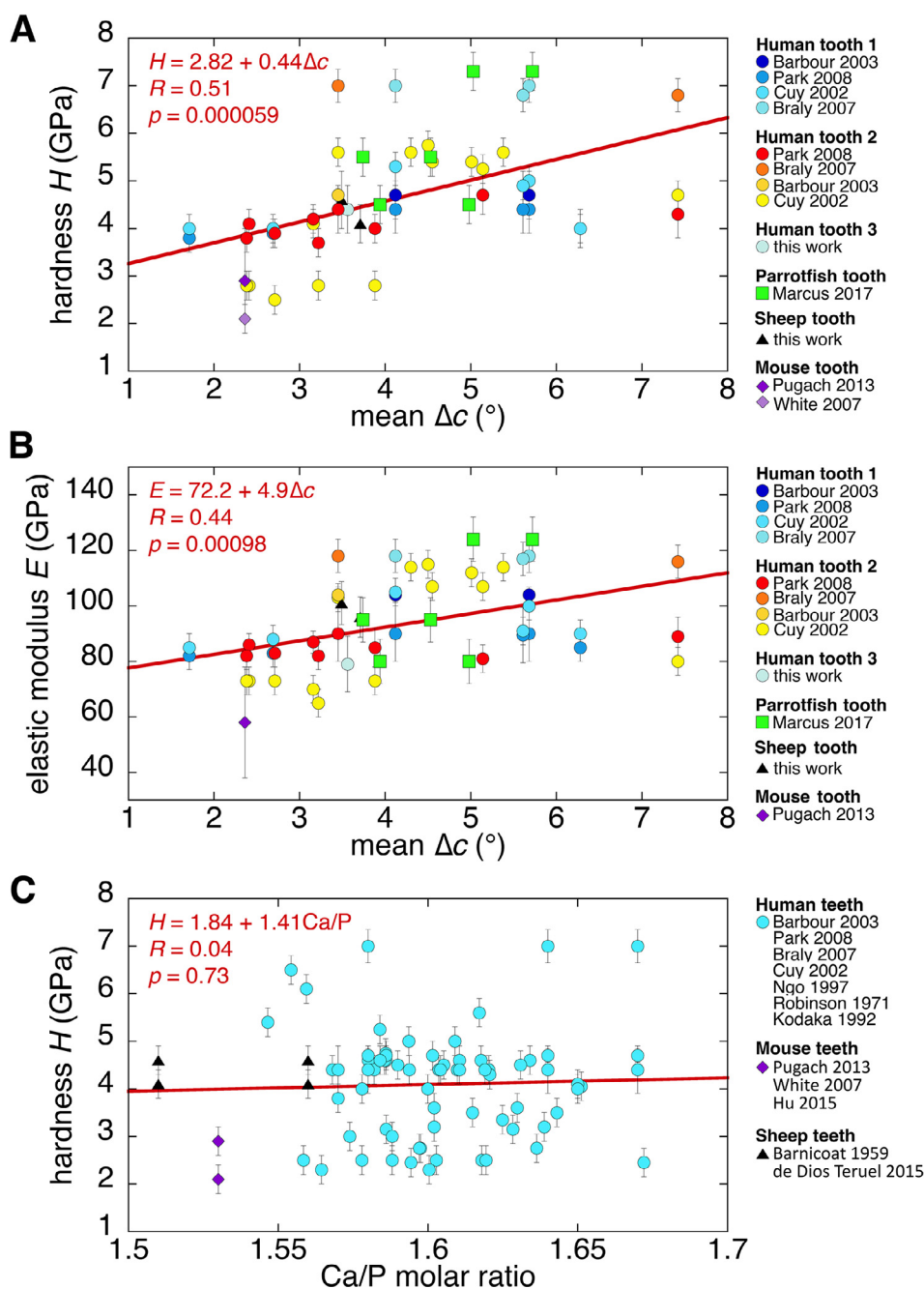
Fig. 7. The hardness (A) and elastic modulus (B) positively correlate with the mean misorientation Δc. The error bars represent ± 1 standard deviation. The correlation coefficients for the linear fits are $R = 0.51$ and $R = 0.44$ for H and E, respectively. Both correlation coefficients for H and E are significantly different from 0, with $p = 0.000059$ and $p = 0.00098$, respectively. The shape of the datapoints indicate the species, and the color indicates the reference from which the H and E values were taken, as indicated by the legend. Three different human teeth were analyzed for misorientation Δc in many different locations of each tooth, and their markers and corresponding H and E references are grouped together under a bold heading in the legend. (C) The hardness does not correlate with the Ca/P molar ratio, thus the linear fit yields a correlation coefficient $R = 0.04$ and $p = 0.73$, indicating that the correlation coefficient is not significantly different from 0.

The correlation between hardness and mean misorientation observed here in the $2°-8°$ angle range shows that the more misoriented, the harder the enamel is. There must therefore be a peak for mechanical performances, somewhere between $8°$ and $30°$, which is optimal for hardness and toughness. Such angles do not occur in enamel, thus other systems must be explored to fully characterize these intriguing structure-properties relationships. For now, we can only constrain the position of the best angle to be within the $8°-30°$ range. Eight degrees is the highest mean misorientation angle observed in enamel(oid)s, where the H-misorientation correlation is still clearly increasing. $30°$ is the full width of the misorientation histograms in Fig. 6 measured in all enamel(oid)s, which is surprisingly similar to that observed in coral skeletons ($35°$) [100,101], in the vaterite spicules of ascidians ($30°$) [110], and in mollusk shell nacre ($30°$) [111,112].

In addition to misorientation, composition also has an appreciable impact on the hardness of enamel. Previous studies have shown that the mineral density is the highest at the tooth surface and decreases toward the DEJ [12,84], and Akkus *et al.* have shown that across teeth from different individuals, there is a strong corre-

lation between mineral content and hardness [113]. Other studies make the connection between decreased organic content and increased hardness for human [114] and mouse enamel [49], when comparing native enamel with enamel that has been bleached, or otherwise treated to remove organics.

Concentration of trace elements that are substituted in the apatite, fluorine in particular, have also been shown to vary in enamel [13,107] and to impact the hardness [115-117]. DeRocher *et al.* 2020 have even found compositional variation within a single nanocrystal where a single nanocrystal has a shell comprised of minimally substituted HAP and a core made of a magnesium enriched layer surrounding a sodium, fluorine, and carbonate enriched center. These compositional gradients are hypothesized to impact the mechanical resilience of enamel [131]. Thus, both composition and misorientation play a role in the mechanical properties of enamel, but further research is needed to determine the relative contributions of these two factors, and whether or not they are synergistic.

The correlation between hardness or and elastic modulus and misorientation observed in Fig. 7 reveals a structure-function relationship not previously considered. Interestingly, in human enamel, high concentrations of organic material are found at the interface of strongly misoriented crystals, similar to the 47° misorientation that did not deflect cracks in MD simulations [71]. It is well known that discontinuous mechanical properties at interfaces deflect cracks, e.g. at organic-mineral interfaces, as observed in sponge spicules, nacre, and sea urchin teeth [118-120]. The organic sheet at the rod-interrod boundaries in human enamel likely play similar roles where, according to MD simulations [71], this is most needed. While the misorientations observed here are relatively small (2°–8°), they represent a widespread nanoscale feature across vertebrate species, and thus likely further contribute to improving enamel's mechanical performance. Just as the structure is hierarchical, so too are the crack deflection mechanisms. The small misorientations provide this crack deflection between adjacent nanocrystals, while the organics between the rods provide a crack deflection mechanism at the rod level. At higher structural levels, decussation patterns, placement of different enamel types, and even tooth shape itself provide enhanced mechanical performance [17,75,76,87].

4. Materials and methods

4.1. Sample preparation

The sheep tooth sample is an unworn lower left first molar (LLM1) from a Finn x Dorset cross breed ewe raised at the Cornell Sheep Program by Mike Thonney and Mary Smith. The age at death was 88 days. A tooth from a young sheep was used as it is less likely to have cracks, carries, or other defects due to age-related wear. The tooth was extracted with a Dremel saw, immersed in 70% ethanol, and embedded in polymethyl methacrylate. Embedded teeth were sectioned across the mesial lophs (analogous to cusps) and polished so that outer enamel surface, DEJ, dentin and pulp tissues are visible. A small portion at the tip of the loph was cut and as much polymethyl methacrylate as possible was trimmed from the cut tooth and re-embedded in Epofix (EMS, Hatfield, PA) to prevent outgassing under high vacuum conditions.

One of the human molar samples not previously published was obtained from the Department of Oral Surgery, University of Pittsburgh School of Dental Medicine, and as such is exempt from IRB approval. The tooth was cut perpendicular to the biting surface and was embedded in Epofix (EMS, Hatfield, PA).

Both teeth were ground with 320, 400, 600, and 1000 grit SiC paper (Buehler, Lake Bluff, IL and polished with 300 nm and then 50 nm alumina suspensions (Buehler, Lake Bluff, IL), with 1 g/L cal-

cium chloride used at each step to prevent dissolution. The samples were cleaned, air-dried, and coated in 1 nm Pt in area of interest and 40 nm elsewhere while spinning and tilting [121].

4.2. PIC mapping

PIC mapping was performed using the PEEM3 microscope at the 11.0.1 beamline at the Advanced Light Source (ALS) at Lawrence Berkeley National Lab. A stack of 38 images was acquired at 19 different x-ray polarizations [67–69,102] with minimal charging [122] and radiation damage [123]; one at 0.2 eV below the Ca L-edge peak 1 and the other at 0.2 eV above peak 1 [70]. The images were imported into PEEMvision and aligned if necessary, then the above peak images were digitally divided by the corresponding below peak images to increase the dichroic contrast, reducing the stack to 19 images, one for each polarization. Each pixel in the stack contains intensity versus polarization information that can be fit to a cosine squared, Malus' law relationship. The fit parameters provide orientation information, namely the in-plane and out-of-plane angles with respect to the polarization plane of the x-rays that are incident from the right at an angle of 30° from the vertically mounted sample surface. The in-plane angles are displayed by the hues assigned in the color bar in Figs. 4 and 5. The out-of-plane angles are displayed such that crystals oriented directly into the x-rays and thus are fully out of the polarization plane are black and crystals that are oriented completely within the polarization plane are full brightness. Thus, a crystal with its *c*-axis oriented vertically with respect to the sample would appear as full brightness cyan in a PIC map as the vertical direction coincides in the image and polarization planes, but a crystal that appears as full brightness magenta and yellow in a PIC map would have their *c*-axes oriented −60° from vertical, 60° in front of the image plane and +60° from vertical, 30° behind the image plane respectively. PIC maps were created from the 19-image stack using the GG macros. For the human, mouse, and sheep enamel PIC maps, a large area composite map was created from an array of overlapping, individual PIC maps stitched together in Adobe Photoshop® CC 2017 [99].

4.3. Angular distances

The angular distance between adjacent pixels in PIC maps in Fig. 1 were calculated by taking the dot product of the in-plane and out-of-plane angles of adjacent pixels based on the RGB values of the pixels [71]. The data were plotted in MATLAB (MathWorks, Natick, MA) as follows: the angular distances binned every 0.5° and the frequency of each bin was expressed as a percent of the total number of pixel pairs to produce the histograms in Fig. 2, with the mean misorientation Δc calculated and displayed directly on the plot. After importing all histograms into Adobe Photoshop® CC 2017, the mean misorientation Δc was displayed on the plot with a thin black line at the appropriate location.

4.4. Nanoindentation

We used a Bruker Hysitron TI-950 Triboindenter equipped with a Berkovich probe at the University of Wisconsin-Madison (Madison, WI, USA) to measure the hardness and elastic modulus of one of the human tooth samples and the sheep tooth. We used a load-control multiload protocol, which consisted of 9 partial loading curves; each having 4 segments: an initial 1 second hold, a loading segment, a 5 second hold, and a partial unloading to 30% of the max load, before moving to the next partial indent. The peak loads of the 9 partial indents were 160 μN, 360 μN, 640 μN, 1000 μN, 1440 μN, 1960 μN, 2560 μN, 3240 μN, and 4000 μN. To more accurately detect the surface and define the zeroed depth and

load, each nanoindentation was preceded by pre-nanoindent liftoff and approach segments. To account for any potential edge effects and displacements of the tooth sample into the compliant embedment during nanoindentation, the structural compliance method was utilized following references [124,125]. In brief, for each multiload nanoindentation the load-dependent stiffness was used to create a SYS plot (total compliance*load$^{1/2}$ vs. load$^{1/2}$) and the structural compliance was calculated from its slope. The structural compliance was then used to correct the corresponding load-depth trace before the elastic modulus and hardness were calculated for each unloading segment using the Oliver and Pharr method [126]. To avoid surface roughness effects and the effects of probe tip imperfections, only the E and H values associated with contact depths over 100 nm were averaged together. Loading curves where the pre-nanoindent liftoff and approach segments did not overlap, or the load-depth trace had some other abnormality were excluded from the analysis.

4.5. Correlation, probability, and significance

We plotted the hardness, measured here or previously, versus the mean misorientation Δc for each PIC map, for 54 distinct H-Δc datapoints ($n = 54$). We fitted a line to the data using least squares linear regression. The correlation coefficient was calculated using Kaleidagraph® 4.5.2, which uses the following formula: $R = \frac{n\sum \Delta c * H - \sum \Delta c * \sum H}{\sqrt{(n\sum \Delta c^2 - (\sum \Delta c)^2)(n\sum H^2 - (\sum H)^2)}}$ [127]. We calculated the significance of the correlation coefficient by using a Fisher transform, $z_f = \frac{1}{2} * ln\frac{1+R}{1-R}$; $\sigma_f = \frac{1}{\sqrt{n-3}}$, where z_f is the mean of the approximately normal Fisher distribution, R is the correlation coefficient, σ_f is the variance of the Fisher distribution, and n is the number of data points [127]. We used the parameters z_f and σ_f in MATLAB (MathWorks, Natick, MA) using the built-in z-test function to test the null hypothesis ($R = 0$) at a significance level of 5%. The value of p is calculated according to the following formula: $p = 1 - \int_{-z}^{z} [\frac{1}{\sigma_f\sqrt{2\pi}} e^{-\frac{1}{2}(\frac{x-0}{\sigma_f})^2}]dx$, where z_f and σ_f are defined above, x is an integration variable, and $z = \frac{z_f}{\sigma_f}$ is the z-score, which is the number of standard deviations away from the mean with respect to a standard normal distribution with the mean = 0 and standard deviation $\sigma = 1$ (expressed as $z\sigma$ significance). If the computed probability p is below 0.05 ($p < 0.05$), then the null hypothesis is rejected, and the correlation coefficient being tested is significantly different from zero. The same mathematical procedure was used to compute the R and p values for E vs. Δc ($n = 53$) and H vs. Ca/P ($n = 79$) and thus determine their significance.

Declaration of Competing Interest

The authors delcare no conflict of interest.

Acknowledgements

References

[1] G. Cuvier, Animal Kingdom, arranged according to its organization, forming the basis for a natural history of animals, and introduction to comparative anatomy, Amen Corner (1840).

[2] W.E. Reif, Morphologie und Ultrastruktur des Hai-"Schmelzes", Zool. Scr. 2 (5-6) (1974) 231–250.

[3] U.G. Wegst, H. Bai, E. Saiz, A.P. Tomsia, R.O. Ritchie, Bioinspired structural materials, Nat Mater 14 (1) (2015) 23–36.

[4] J. Elliott, D. Holcomb, R. Young, Infrared determination of the degree of substitution of hydroxyl by carbonate ions in human dental enamel, Calcif. Tissue Int. 37 (4) (1985) 372–375.

[5] F. Driessens, The mineral in bone, dentin and tooth enamel, Bulletin des sociétés chimiques belges 89 (8) (1980) 663–689.

[6] R. Young, Biological apatite vs hydroxyapatite at the atomic level, Clin. Orthop. Relat. Res. (113) (1975) 249–262.

[7] R. Young, P. Mackie, Crystallography of human tooth enamel: initial structure refinement, Mater Res Bull 15 (1) (1980) 17–29.

[8] J. de Dios Teruel, A. Alcolea, A. Hernández, A.J.O. Ruiz, Comparison of chemical composition of enamel and dentine in human, bovine, porcine and ovine teeth, Arch. Oral Biol. 60 (5) (2015) 768–775.

[9] C. Robinson, J. Weatherell, A. Hallsworth, Variation in composition of dental enamel within thin ground tooth sections, Caries Res. 5 (1) (1971) 44–57.

[10] C. Barnicoat, Wear in sheep's teeth: VI. Chemical composition of teeth of grazing sheep, New Zealand Journal of Agricultural Research 2 (5) (1959) 1025–1040.

[11] H. Ngo, J. Ruben, J. Arends, D. White, G. Mount, M. Peters, R. Faller, A. Pfarrer, Electron probe microanalysis and transverse microradiography studies of artificial lesions in enamel and dentin: a comparative study, Adv. Dent. Res. 11 (4) (1997) 426–432.

[12] T. Kodaka, K. Debari, M. Yamada, M. Kuroiwa, Correlation between microhardness and mineral content in sound human enamel, Caries Res. 26 (2) (1992) 139–141.

[13] J. Weatherell, C. Robinson, A. Hallsworth, Variations in the chemical composition of human enamel, J. Dent. Res. 53 (2) (1974) 180–192.

[14] W.V. Koenigswald, W. Clemens, Levels of complexity in the microstructure of mammalian enamel and their application in studies of systematics, Scanning Microsc. 6 (1) (1992) 195–217 discussion 217-8.

[15] W.R. Trumble, A. Stevenson, L. Brown, Shorter Oxford English Dictionary on Historical Principles: NZ, Oxford University Press, 2003.

[16] Y. Kaifu, K. Kasai, G.C. Townsend, L.C. Richards, Tooth wear and the "design" of the human dentition: a perspective from evolutionary medicine, American Journal of Physical Anthropology: The Official Publication of the American Association of Physical Anthropologists 122 (S37) (2003) 47–61.

[17] A. Barani, A.J. Keown, M.B. Bush, J.J.-W. Lee, B.R. Lawn, Role of tooth elongation in promoting fracture resistance, J Mech Behav Biomed Mater 8 (2012) 37–46.

[18] J. Damuth, C.M. Janis, On the relationship between hypsodonty and feeding ecology in ungulate mammals, and its utility in palaeoecology, Biological Reviews 86 (3) (2011) 733–758.

[19] A. Carr, I.R. Tibbetts, A. Kemp, R. Truss, J. Drennan, Inferring parrotfish (Teleostei: scaridae) pharyngeal mill function from dental morphology, wear, and microstructure, J. Morphol. 267 (10) (2006) 1147–1156.

[20] P.S. Ungar, Mammal teeth: origin, evolution, and Diversity, JHU Press, 2010.

[21] J. Catón, H.-.U. Luder, M. Zoupa, M. Bradman, G. Bluteau, A.S. Tucker, O. Klein, T.A. Mitsiadis, Enamel-free teeth, Tbx1 deletion affects amelogenesis in rodent incisors, Dev. Biol. 328 (2) (2009) 493–505.

[22] J.D. Bartlett, B. Ganss, M. Goldberg, J. Moradian-Oldak, M.L. Paine, M.L. Snead, X. Wen, S.N. White, Y.L. Zhou, Protein–protein interactions of the developing enamel matrix, Curr. Top. Dev. Biol. 74 (2006) 57–115.

[23] J. Moradian-Oldak, Protein-mediated enamel mineralization, Frontiers in bioscience, a journal and virtual library (1996) 17.

[24] V. Uskoković, M. Kim, W. Li, S. Habelitz, Enzymatic processing of amelogenin during continuous crystallization of apatite, J Mater Res 23 (12) (2008) 3184–3195.

[25] G.W. Marshall Jr, S.J. Marshall, J.H. Kinney, M. Balooch, The dentin substrate: structure and properties related to bonding, J Dent 25 (6) (1997) 441–458.

[26] M. Goldberg, A.B. Kulkarni, M. Young, A. Boskey, Dentin: structure, Composition and Mineralization: the role of dentin ECM in dentin formation and mineralization, Front Biosci (Elite Ed) 3 (2011) 711.

[27] P. Zaslansky, A.A. Friesem, S. Weiner, Structure and mechanical properties of the soft zone separating bulk dentin and enamel in crowns of human teeth: insight into tooth function, J. Struct. Biol. 153 (2) (2006) 188–199.

[28] T. Yamamoto, T. Hasegawa, T. Yamamoto, H. Hongo, N. Amizuka, Histology of human cementum: its structure, function, and development, Japanese dental science review 52 (3) (2016) 63–74.

[29] G. Cuny, G. Guinot, S. Enault, Evolution of Dental Tissues and Paleobiology in Selachians, Elsevier, 2018.

[30] I. Sasagawa, M. Ishiyama, H. Yokosuka, M. Mikami, Teeth and ganoid scales in Polypterus and Lepisosteus, the basic actinopterygian fish: an approach to understand the origin of the tooth enamel, Journal of Oral Biosciences 55 (2) (2013) 76–84.

[31] E.D. Yilmaz, J. Koldehoff, G.A. Schneider, On the systematic documentation of the structural characteristics of bovine enamel: a critic to the protein sheath concept, Dental Materials 34 (10) (2018) 1518–1530.

[32] M.C. Maas, E.R. Dumont, Built to last: the structure, function, and evolution of primate dental enamel, Evolutionary Anthropology: issues, News, and Reviews: issues, News, and Reviews 8 (4) (1999) 133–152.

[33] G. Daculsi, J. Menanteau, L. Kerebel, D. Mitre, Length and shape of enamel crystals, Calcif. Tissue Int. 36 (1) (1984) 550–555.

[34] M.C. Maas, Enamel structure and microwear: an experimental study of the response of enamel to shearing force, Am. J. Phys. Anthropol. 85 (1) (1991) 31–49.

[35] A. Boyde, Electron microscopic observations relating to the nature and development of prism decussation in mammalian dental enamel, Group. Int. Rech. Sc. Stomat. Bull 12 (1969) 151–207.

[36] A. Boyde, A non-destructive survey of prism packing patterns in primate enamels, Tooth enamel (1984) 417–421.

[37] A. Boyde, L. Martin, Tandem scanning reflected light microscopy of primate enamel, Scanning Microsc. 1 (4) (1987) 1935–1948.

[38] A. Boyde, The Development of Enamel Structure, SAGE Publications, 1967.

[39] A. Boyde, Dependence of rate of physical erosion on orientation and density in mineralised tissues, Anat. Embryol. 170 (1) (1984) 57–62.

[40] D.G. Gantt, D. Pilbeam, G.P. Steward, Hominoid enamel prism patterns, Science 198 (4322) (1977) 1155–1157.

[41] A. Boyde, L. Martin, Enamel microstructure determination in hominoid and cercopithecoid primates, Anat. Embryol. 165 (2) (1982) 193–212.

[42] S. Risnes, Growth tracks in dental enamel, J. Hum. Evol. 35 (4–5) (1998) 331–350.

[43] P. Tafforeau, J.P. Zermeno, T.M. Smith, Tracking cellular-level enamel growth and structure in 4D with synchrotron imaging, J. Hum. Evol. 62 (3) (2012) 424–428.

[44] S. Habelitz, S. Marshall, G. Marshall Jr., M. Balooch, Mechanical properties of human dental enamel on the nanometre scale, Arch. Oral Biol. 46 (2) (2001) 173–183.

[45] F.Z. Cui, J. Ge, New observations of the hierarchical structure of human enamel, from nanoscale to microscale, J Tissue Eng Regen Med 1 (3) (2007) 185–191.

[46] H. Kierdorf, U. Kierdorf, K. Frölich, C. Witzel, Lines of evidence–incremental markings in molar enamel of Soay sheep as revealed by a fluorochrome labeling and backscattered electron imaging study, PLoS ONE 8 (9) (2013).

[47] S.P. Lyngstadaas, C.B. Møinichen, S. Risnes, Crown morphology, enamel distribution, and enamel structure in mouse molars, The Anatomical Record: An Official Publication of the American Association of Anatomists 250 (3) (1998) 268–280.

[48] C. Leblond, H. Warshawsky, Dynamics of enamel formation in the rat incisor tooth, J. Dent. Res. 58 (2_suppl) (1979) 950–979.

[49] M. Baldassarri, H. Margolis, E. Beniash, Compositional determinants of mechanical properties of enamel, J. Dent. Res. 87 (7) (2008) 645–649.

[50] A. Jodaikin, S. Weiner, W. Traub, Enamel rod relations in the developing rat incisor, J. Ultrastruct. Res. 89 (3) (1984) 324–332.

[51] L.M. Gordon, M.J. Cohen, K.W. MacRenaris, J.D. Pasteris, T. Seda, D. Joester, Amorphous intergranular phases control the properties of rodent tooth enamel, Science 347 (6223) (2015) 746–750.

[52] A.G. Carr, Microstructure and mechanical properties of parrotfish pharyngeal teeth, (2003).

[53] M.A. Marcus, S. Amini, C.A. Stifler, C.-Y. Sun, N. Tamura, H.A. Bechtel, D.Y. Parkinson, H.S. Barnard, X.X. Zhang, J.I. Chua, Parrotfish teeth: stiff biominerals whose microstructure makes them tough and abrasion-resistant to bite stony corals, ACS Nano 11 (12) (2017) 11856–11865.

[54] A. Carr, A. Kemp, I. Tibbetts, R. Truss, J. Drennan, Microstructure of pharyngeal tooth enameloid in the parrotfish Scarus rivulatus (Pisces: scaridae), J Microsc 221 (1) (2006) 8–16.

[55] G. Daculsi, B. Kerebel, High-resolution electron microscope study of human enamel crystallites: size, shape, and growth, J. Ultrastruct. Res. 65 (2) (1978) 163–172.

[56] A. Marshall, K. Lawless, TEM study of the central dark line in enamel crystallites, J. Dent. Res. 60 (10) (1981) 1773–1782.

[57] J. Xue, A. Zavgorodniy, B. Kennedy, M. Swain, W. Li, X-ray microdiffraction, TEM characterization and texture analysis of human dentin and enamel, J Microsc 251 (2) (2013) 144–153.

[58] H. Eimar, E. Ghadimi, B. Marelli, H. Vali, S.N. Nazhat, W.M. Amin, J. Torres, O. Ciobanu, R.F.A. Junior, F. Tamimi, Regulation of enamel hardness by its crystallographic dimensions, Acta Biomater 8 (9) (2012) 3400–3410.

[59] L.M. Simmons, M. Al-Jawad, S.H. Kilcoyne, D.J. Wood, Distribution of enamel crystallite orientation through an entire tooth crown studied using synchrotron X-ray diffraction, Eur. J. Oral Sci. 119 (2011) 19–24.

[60] M. Al-Jawad, O. Addison, M.A. Khan, A. James, C.J. Hendriksz, Disruption of enamel crystal formation quantified by synchrotron microdiffraction, J Dent 40 (12) (2012) 1074–1080.

[61] M. Al-Jawad, L. Simmons, A. Steuwer, S.H. Kilcoyne, R. Shore, R. Cywinski, D.J. Wood, Three dimensional mapping of texture in dental enamel, Key engineering materials, Trans Tech Publ (2008) 877–880.

[62] M. Al-Jawad, A. Steuwer, S.H. Kilcoyne, R.C. Shore, R. Cywinski, D.J. Wood, 2D mapping of texture and lattice parameters of dental enamel, Biomaterials 28 (18) (2007) 2908–2914.

[63] L. Raue, N. Gersdorff, M. Rödiger, H. Klein, New insights in prism orientation within human enamel, Arch. Oral Biol. 57 (3) (2012) 271–276.

[64] S. Siddiqui, P. Anderson, M. Al-Jawad, Recovery of crystallographic texture in remineralized dental enamel, PLoS ONE 9 (10) (2014).

[65] Y. Fan, Z. Sun, J. Moradian-Oldak, Controlled remineralization of enamel in the presence of amelogenin and fluoride, Biomaterials 30 (4) (2009) 478–483.

[66] A. Koblischka-Veneva, M.R. Koblischka, J. Schmauch, M. Hannig, Human dental enamel: a natural nanotechnology masterpiece investigated by TEM and t-EBSD, Nano Res 11 (7) (2018) 3911–3921.

[67] R.T. DeVol, R.A. Metzler, L. Kabalah-Amitai, B. Pokroy, Y. Politi, A. Gal, L. Addadi, S. Weiner, A. Fernandez-Martinez, R. Demichelis, Oxygen spectroscopy and polarization-dependent imaging contrast (PIC)-mapping of calcium carbonate minerals and biominerals, The Journal of Physical Chemistry B 118 (28) (2014) 8449–8457.

[68] R.A. Metzler, M. Abrecht, R.M. Olabisi, D. Ariosa, C.J. Johnson, B.H. Frazer, S.N. Coppersmith, P.U.P.A. Gilbert, Architecture of columnar nacre, and implications for its formation mechanism, Phys. Rev. Lett. 98 (26) (2007) 268102.

[69] R.A. Metzler, D. Zhou, M. Abrecht, J.-W. Chiou, J. Guo, D. Ariosa, S.N. Coppersmith, P.U.P.A. Gilbert, Polarization-dependent imaging contrast in abalone shells, Physical Review B 77 (6) (2008) 064110.

[70] C.A. Stifler, N.K. Wittig, M. Sassi, C.-Y. Sun, M.A. Marcus, H. Birkedal, E. Beniash, K.M. Rosso, P.U.P.A. Gilbert, X-ray linear dichroism in apatite, J. Am. Chem. Soc. 140 (37) (2018) 11698–11704.

[71] E. Beniash, C.A. Stifler, C.-Y. Sun, G.S. Jung, Z. Qin, M.J. Buehler, P.U.P.A. Gilbert, The hidden structure of human enamel, Nat Commun 10 (1) (2019) 1–13.

[72] Y.-J. Wu, Y.-H. Tseng, J.C. Chan, Morphology control of fluorapatite crystallites by citrate ions, Cryst Growth Des 10 (10) (2010) 4240–4242.

[73] B. An, R. Wang, D. Zhang, Role of crystal arrangement on the mechanical performance of enamel, Acta Biomater 8 (10) (2012) 3784–3793.

[74] S. White, W. Luo, M. Paine, H. Fong, M. Sarikaya, M. Snead, Biological organization of hydroxyapatite crystallites into a fibrous continuum toughens and controls anisotropy in human enamel, J. Dent. Res. 80 (1) (2001) 321–326.

[75] I. Scheider, T. Xiao, E. Yilmaz, G.A. Schneider, N. Huber, S. Bargmann, Damage modeling of small-scale experiments on dental enamel with hierarchical microstructure, Acta Biomater 15 (2015) 244–253.

[76] L.H. He, M.V. Swain, Understanding the mechanical behaviour of human enamel from its structural and compositional characteristics, J Mech Behav Biomed Mater 1 (1) (2008) 18–29.

[77] S. Varga, S. Spalj, M. Lapter Varga, S. Anic Milosevic, S. Mestrovic, M. Slaj, Maximum voluntary molar bite force in subjects with normal occlusion, The European Journal of Orthodontics 33 (4) (2011) 427–433.

[78] L.H. He, M.V. Swain, Enamel—A "metallic-like" deformable biocomposite, J Dent 35 (5) (2007) 431–437.

[79] A. Braly, L. Darnell, A. Mann, M. Teaford, T. Weihs, The effect of prism orientation on the indentation testing of human molar enamel, Arch. Oral Biol. 52 (9) (2007) 856–860.

[80] S. Rasmussen, R. Patchin, Fracture properties of human enamel and dentin in an aqueous environment, J. Dent. Res. 63 (12) (1984) 1362–1368.

[81] E.D. Yilmaz, H. Jelitto, G.A. Schneider, Uniaxial compressive behavior of micro-pillars of dental enamel characterized in multiple directions, Acta Biomater 16 (2015) 187–195.

[82] D. Shimizu, G.A. Macho, I.R. Spears, Effect of prism orientation and loading direction on contact stresses in prismatic enamel of primates: implications for interpreting wear patterns, American Journal of Physical Anthropology: The Official Publication of the American Association of Physical Anthropologists 126 (4) (2005) 427–434.

[83] S.F. Ang, M. Saadatmand, M.V. Swain, A. Klocke, G.A. Schneider, Comparison of mechanical behaviors of enamel rod and interrod regions in enamel, J Mater Res 27 (2) (2012) 448–456.

[84] J.L. Cuy, A.B. Mann, K.J. Livi, M.F. Teaford, T.P. Weihs, Nanoindentation mapping of the mechanical properties of human molar tooth enamel, Arch. Oral Biol. 47 (4) (2002) 281–291.

[85] A. Barani, M.B. Bush, B.R. Lawn, Effect of property gradients on enamel fracture in human molar teeth, J Mech Behav Biomed Mater 15 (2012) 121–130.

[86] S. Park, D.H. Wang, D. Zhang, E. Romberg, D. Arola, Mechanical properties of human enamel as a function of age and location in the tooth, Journal of Materials Science: Materials in Medicine 19 (6) (2008) 2317–2324.

[87] E.D. Yilmaz, G.A. Schneider, M.V. Swain, Influence of structural hierarchy on the fracture behaviour of tooth enamel, Philosophical Transactions of the Royal Society A: mathematical, Physical and Engineering Sciences 373 (2038) (2015) 20140130.

[88] H. Chai, J.J.-W. Lee, P.J. Constantino, P.W. Lucas, B.R. Lawn, Remarkable resilience of teeth, Proceedings of the National Academy of Sciences 106 (18) (2009) 7289–7293.

[89] S. Lees, F. Rollins Jr., Anisotropy in hard dental tissues, J Biomech 5 (6) (1972) 557–566.

[90] I. Spears, R. Van Noort, R. Crompton, G. Cardew, I. Howard, The effects of enamel anisotropy on the distribution of stress in a tooth, J. Dent. Res. 72 (11) (1993) 1526–1531.

[91] M. Yahyazadehfar, D. Bajaj, D.D. Arola, Hidden contributions of the enamel rods on the fracture resistance of human teeth, Acta Biomater 9 (1) (2013) 4806–4814.

[92] L.H. He, N. Fujisawa, M.V. Swain, Elastic modulus and stress–strain response of human enamel by nano-indentation, Biomaterials 27 (24) (2006) 4388–4398.

[93] Z.-j. Cheng, X.-m. Wang, J. Ge, J.-x. Yan, N. Ji, Ll. Tian, F.-z. Cui, The mechanical anisotropy on a longitudinal section of human enamel studied by nanoindentation, Journal of Materials Science: Materials in Medicine 21 (6) (2010) 1811–1816.

[94] D. Zaytsev, P. Panfilov, Anisotropy of the mechanical properties of human dental enamel, Mater Lett 159 (2015) 428–431.

[95] T. Aoba, The effect of fluoride on apatite structure and growth, Critical Reviews in Oral Biology & Medicine 8 (2) (1997) 136–153.

[96] E. Menendez-Proupin, S. Cervantes-Rodríguez, R. Osorio-Pulgar, M. Franco-Cisterna, H. Camacho-Montes, M. Fuentes, Computer simulation of elastic constants of hydroxyapatite and fluorapatite, J Mech Behav Biomed Mater 4 (7) (2011) 1011–1020.

[97] L.B. Whitenack, D.C. Simkins Jr, P.J. Motta, M. Hirai, A. Kumar, Young's modulus and hardness of shark tooth biomaterials, Arch. Oral Biol. 55 (3) (2010) 203–209.

[98] P.-Y. Chen, J. Schirer, A. Simpson, R. Nay, Y.-S. Lin, W. Yang, M.I. Lopez, J. Li, E.A. Olevsky, M.A. Meyers, Predation versus protection: fish teeth and scales evaluated by nanoindentation, J Mater Res 27 (1) (2012) 100–112.

[99] S. O'Brien, A.J. Keown, P. Constantino, Z. Xie, M.B. Bush, Revealing the structural and mechanical characteristics of ovine teeth, J Mech Behav Biomed Mater 30 (2014) 176–185.

[100] C.-Y. Sun, M.A. Marcus, M.J. Frazier, A.J. Giuffre, T. Mass, P.U. Gilbert, Spherulitic growth of coral skeletons and synthetic aragonite: nature's three-dimensional printing, ACS Nano 11 (7) (2017) 6612–6622.

[101] C.-Y. Sun, L. Gránásy, C.A. Stifler, T. Zaquin, R.V. Chopdekar, N. Tamura, J.C. Weaver, J.A.Y. Zhang, S. Goffredo, G. Falini, M.A. Marcus, T. Pusztai, V. Schoeppler, T. Mass, P.U.P.A. Gilbert, Crystal nucleation and growth in spherulites revealed by coral skeletons, Acta Biomater (This issue) (2020).

[102] P.U.P.A. Gilbert, A. Young, S.N. Coppersmith, Measurement of c-axis angular orientation in calcite (CaCO3) nanocrystals using X-ray absorption spectroscopy, Proceedings of the National Academy of Sciences 108 (28) (2011) 11350–11355.

[103] M. Mukaka, Statistics corner: a guide to appropriate use of correlation in medical research, Malawi Medical Journal 24 (3) (2012) 69–71.

[104] M. Pugach, C. Suggs, Y. Li, J. Wright, A. Kulkarni, J. Bartlett, C. Gibson, M180 amelogenin processed by MMP20 is sufficient for decussating murine enamel, J. Dent. Res. 92 (12) (2013) 1118–1122.

[105] S.N. White, M.L. Paine, A.Y. Ngan, V.G. Miklus, W. Luo, H. Wang, M.L. Snead, Ectopic expression of dentin sialoprotein during amelogenesis hardens bulk enamel, Journal of Biological Chemistry 282 (8) (2007) 5340–5345.

[106] M.E. Barbour, D.M. Parker, G.C. Allen, K.D. Jandt, Human enamel dissolution in citric acid as a function of pH in the range 2.30≤ pH≤ 6.30–a nanoindentation study, Eur. J. Oral Sci. 111 (3) (2003) 258–262.

[107] Y. Hu, C.E. Smith, A.S. Richardson, J.D. Bartlett, J.C. Hu, J.P. Simmer, MMP20, KLK4, and MMP20/KLK4 double null mice define roles for matrix proteases during dental enamel formation, Mol Genet Genomic Med 4 (2) (2016) 178–196.

[108] S. Saber-Samandari, K.A. Gross, Micromechanical properties of single crystal hydroxyapatite by nanoindentation, Acta Biomater 5 (6) (2009) 2206–2212.

[109] A. Zamiri, S. De, Mechanical properties of hydroxyapatite single crystals from nanoindentation data, J Mech Behav Biomed Mater 4 (2) (2011) 146–152.

[110] B. Pokroy, L. Kabalah-Amitai, I. Polishchuk, R.T. DeVol, A.Z. Blonsky, C.-Y. Sun, M.A. Marcus, A. Scholl, P.U.P.A. Gilbert, Narrowly distributed crystal orientation in biomineral vaterite, Chemistry of Materials 27 (19) (2015) 6516–6523.

[111] I.C. Olson, A.Z. Blonsky, N. Tamura, M. Kunz, B. Pokroy, C.P. Romao, M.A. White, P.U.P.A. Gilbert, Crystal nucleation and near-epitaxial growth in nacre, J. Struct. Biol. 184 (3) (2013) 454–463.

[112] P.U.P.A. Gilbert, K.D. Bergmann, C.E. Myers, M.A. Marcus, R.T. DeVol, C.-Y. Sun, A.Z. Blonsky, E. Tamre, J. Zhao, E.A. Karan, Nacre tablet thickness records formation temperature in modern and fossil shells, Earth Planet. Sci. Lett. 460 (2017) 281–292.

[113] A. Akkus, D. Karasik, R. Roperto, Correlation between micro-hardness and mineral content in healthy human enamel, J Clin Exp Dent 9 (4) (2017) e569.

[114] H.M. Elfallah, L.E. Bertassoni, N. Charadram, C. Rathsam, M.V. Swain, Effect of tooth bleaching agents on protein content and mechanical properties of dental enamel, Acta Biomater 20 (2015) 120–128.

[115] D. Chachra, C. Turner, A. Dunipace, M. Grynpas, The effect of fluoride treatment on bone mineral in rabbits, Calcif. Tissue Int. 64 (4) (1999) 345–351.

[116] I. Cacciotti, Cationic and anionic substitutions in hydroxyapatite, Handbook of bioceramics and biocomposites (2016) 145–211.

[117] C. Riedel, E.A. Zimmermann, J. Zustin, M. Niecke, M. Amling, M. Grynpas, B. Busse, The incorporation of fluoride and strontium in hydroxyapatite affects the composition, structure, and mechanical properties of human cortical bone, Journal of Biomedical Materials Research Part A 105 (2) (2017) 433–442.

[118] J. Aizenberg, J.C. Weaver, M.S. Thanawala, V.C. Sundar, D.E. Morse, P. Fratzl, Skeleton of Euplectella sp.: structural hierarchy from the nanoscale to the macroscale, Science 309 (5732) (2005) 275–278.

[119] A. Jackson, J.F. Vincent, R. Turner, The mechanical design of nacre, Proceedings of the Royal society of London. Series B. Biological sciences 234 (1277) (1988) 415–440.

[120] C.E. Killian, R.A. Metzler, Y. Gong, T.H. Churchill, I.C. Olson, V. Trubetskoy, M.B. Christensen, J.H. Fournelle, F. De Carlo, S. Cohen, Self-Sharpening Mechanism of the Sea Urchin Tooth, Adv Funct Mater 21 (4) (2011) 682–690.

[121] G. De Stasio, B.H. Frazer, B. Gilbert, K.L. Richter, J.W. Valley, Compensation of charging in X-PEEM: a successful test on mineral inclusions in 4.4 Ga old zircon, Ultramicroscopy 98 (1) (2003) 57–62.

[122] B. Gilbert, R. Andres, P. Perfetti, G. Margaritondo, G. Rempfer, G. De Stasio, Charging phenomena in PEEM imaging and spectroscopy, Ultramicroscopy 83 (1–2) (2000) 129–139.

[123] T. Parasassi, O. Sapora, A. Giusti, G. De Stasio, G. Ravagnan, Alterations in erythrocyte membrane lipids induced by low doses of ionizing radiation as revealed by 1, 6-diphenyl-1, 3, 5-hexatriene fluorescence lifetime, Int. J. Radiat. Biol. 59 (1) (1991) 59–69.

[124] J. Jakes, C. Frihart, J. Beecher, R. Moon, P. Resto, Z. Melgarejo, O. Suarez, H. Baumgart, A. Elmustafa, D. Stone, Nanoindentation near the edge, J Mater Res 24 (3) (2009) 1016–1031.

[125] J.E. Jakes, C.R. Frihart, J.F. Beecher, R.J. Moon, D. Stone, Experimental method to account for structural compliance in nanoindentation measurements, J Mater Res 23 (4) (2008) 1113–1127.

[126] W.C. Oliver, G.M. Pharr, An improved technique for determining hardness and elastic modulus using load and displacement sensing indentation experiments, J Mater Res 7 (6) (1992) 1564–1583.

[127] D.N.J.J. Salkind, Encyclopedia of Measurement and Statistics, SAGE Publications, Inc, Thousand Oaks, 2006.

[128] Y. Hu, J.C.C. Hu, C.E. Smith, J.D. Bartlett, J.P. Simmer, Kallikrein-related peptidase 4, matrix metalloproteinase 20, and the maturation of murine and porcine enamel, Eur. J. Oral Sci. 119 (2011) 217–225.

[129] L.M. Gordon, D. Joester, Mapping residual organics and carbonate at grain boundaries and the amorphous interphase in mouse incisor enamel, Front Physiol 6 (2015) 57.

[130] T. Popowics, J. Rensberger, S. Herring, Enamel microstructure and microstrain in the fracture of human and pig molar cusps, Arch. Oral Biol. 49 (8) (2004) 595–605.

[131] K.A. DeRocher, P.J.M. Smeets, B.H. Goodge, M.J. Zachman, P.V. Balachandran, L. Stegbauer, M.J. Cohen, L.M. Gordon, J.M. Rondinelli, L.F. Kourkoutis, D. Joester, Chemical gradients in human enamel crystallites, Nature 583 (7814) (2020) 66–71.

[132] K.A. Selvig, A. Halse, Crystal Growth in Rat Incisor Enamel, The Anatomical Record 173 (4) (1972) 453–468.